communications chemistry

A Nature Portfolio journal

Article

https://doi.org/10.1038/s42004-025-01792-9

Unveiling the alkyne-π interaction using metal-organic cage compounds

Check for updates

Junrui Liu[1,2,3], Shujun Ning[1], Ting Chen[1,2,3], Zi-Ang Nan[1,3], Zhe-Ning Chen[1,2,4], Luyao Liu[1,3], Zhu Zhuo[1,3], Qing Li[1,3], Wei Wang[1,2,3] ✉, Lu Zhang[1,2,4] ✉ & You-Gui Huang[1,3,5] ✉

Alkynes play a crucial role in chemical synthesis, bio-imaging, and drug design. Despite their significance, the intermolecular interactions involving alkynes have been largely unexplored. In this work, we unveil the previously overlooked alkyne-π interaction by comparing two zirconocene metal-organic cage compounds. The distinct stacking geometry in the single-crystal structures, coupling with the changes in C ≡ C vibrational signals, confirms the alkyne-π interaction as a genuine intermolecular interaction. Combining with computational studies, we reveal that alkyne-π interactions exert a substantial influence on the spectroscopic properties, despite being energetically less potent than π-π interactions. Our findings extend beyond theoretical implications. A comprehensive survey of the Cambridge Crystallographic Data Centre (CCDC) database corroborates the occurrence of alkyne-π interactions across hundreds of crystal structures, which provides a missing piece for fundamentally rationalizing their properties. Meanwhile, the changing C ≡ C vibrational signals, under alkyne-π interactions, may provide strategies for improving bio-imaging resolutions. It could also serve as a signature for desired alkyne-containing supramolecular structures. These results highlight the potential of alkyne-π interactions in designing functional materials for advanced applications in chemistry and biology.

Non-covalent interactions are essential for sustaining life and performing ubiquitous biological functions[1]. Among different non-covalent interactions, π interactions form a significant category, describing the interactions between aromatic molecules/fragments and nearby chemical groups. Distinguished by the interacting moieties, π–π[2], XH–π[3,4], cation–π[5,6], anion–π[7,8], and lone-pair–π interactions[9–11] have garnered substantial research interests in the past few decades. By strategically manipulating these π interactions, scientists are able to craft intricate supramolecular structures[12–15], achieve precise molecular recognition[16], and produce catalysts with high efficiency that mimic enzymatic functions[17]. The identification of different intermolecular forces creates a strong foundation for innovations within the field of supramolecular chemistry.

Intermolecular interactions are often discovered through gas phase studies or by examining known protein structures[18,19]. The structural features are then corroborated through energy analyses and spectroscopic characterizations to confirm the existence of interactions. Given that many discoveries in this field have been protein-centric, the moieties involved in known π-interactions are frequently observed in biological systems. Examples include aromatic rings, cations, and halogen anions[20–22]. While biological molecular structures have significantly contributed to our understanding of intermolecular interactions, they may not fully reveal the existence of interactions involving less common moieties in nature.

An example of such an overlooked component is the alkyne group. Alkyne groups are not typically found in life-forming molecules, such as amino acids, nucleic acids, and electrolytes. This absence is supported by the "Raman-silent spectral window of cells (1800–2800 cm^{-1})[23], where the characteristic Raman signal of the C≡C stretching vibration is located". The relative invisibility of alkyne groups in biological systems may have led to their underrepresentation in studies of supramolecular interactions. In the literature, few structural descriptions hint at the possible interactions involving alkyne groups. For instance, Siegel et al.[24] described a scenario where "one radical benzene ring sits atop the acetylene of its neighbor", and

[1]CAS Key Laboratory of Design and Assembly of Functional Nanostructures, Fujian Provincial Key Laboratory of Nanomaterials, and State Key Laboratory of Structural Chemistry, Fujian Institute of Research on the Structure of Matter, Chinese Academy of Sciences, Fuzhou, Fujian, China. [2]University of Chinese Academy of Sciences, Beijing, China. [3]Xiamen Key Laboratory of Rare Earth Photoelectric Functional Materials, Xiamen Institute of Rare Earth Materials, Haixi Institutes, Chinese Academy of Sciences, Xiamen, Fujian, China. [4]Fujian Provincial Key Laboratory of Theoretical and Computational Chemistry, Xiamen, Fujian, China. [5]Fujian Science & Technology Innovation Laboratory for Optoelectronic Information of China, Fuzhou, Fujian, China. ✉e-mail: wangwei@fjirsm.ac.cn; luzhang@fjirsm.ac.cn; yghuang@fjirsm.ac.cn

Sakamoto et al.[25] noticed that "an alkyne from an adjacent monomer overlaps with each anthracene". However, none of these studies definitively validate the existence and properties of alkyne-involved intermolecular interactions.

Meanwhile, despite their scarcity in cellular components, alkyne-containing compounds play a pivotal role in biological and medical sciences, as the distinctive C≡C stretching vibration of the probe molecules can be tracked to monitor specific biological processes. For example, alkyne-tagged probes are widely studied for visualizing proteins, nucleic acids, glycans, and other small metabolites, with stimulated Raman scattering (SRS) microscopy[26,27]. Researchers have dedicated to develop protocols and strategies, for enhancing signal resolution and enabling multi-channel imaging[28]. These efforts lead to a diverse library of probes with C≡C stretching signals covering a broad spectrum ranging from 2017 to 2262 cm^{-1}. Meanwhile, besides their utility in bio-imaging, alkyne-containing molecules are also integral to numerous commercially available medications[29]. Notable examples include Mifepristone, used for contraception, and Selegiline, which is prescribed for the treatment of depression, Parkinson's, and Alzheimer's diseases. Given the extensive applications of alkyne-containing molecules in complex biological systems from bioimaging to biomedicine, it is crucial to investigate the intermolecular interactions involving alkyne groups and understand their impact from both chemical and physical perspectives.

In this work, we compare two structurally analogous compounds, **Red-1** and **Orange-1**, containing the same metal-organic cage $\{[Cp_3Zr_3(\mu_3\text{-}O)(\mu_2\text{-}OH)_3]_2L_3\}Cl_2$. By focusing on the interactions between alkyne groups and aromatic rings, we examine their effects on the chemical and physical properties while minimizing the differences introduced by other intermolecular interactions. Experimental evidence and theoretical analysis both suggest that alkyne-π interactions are a genuine intermolecular interaction, pivotal in determining the spectroscopic properties of the compounds. This makes the alkyne-π interaction an intriguing and functional intermolecular interaction.

Result and discussion

Structure description of Red-1 and Orange-1 and identification of an alkyne-π interaction in Red-1

During the synthesis of metal-organic cages (MOCs) with trinuclear zirconium-oxo cluster nodes $\{Cp_3Zr_3(\mu_3\text{-}O)(\mu_2\text{-}OH)_3\}$ (where $Cp = C_5H_5^-$), we obtained two structurally similar compounds. It is well-known that zirconocene MOCs can be synthesized by hydrolyzing zirconium bis(cyclopentadienyl) dichloride ($ZrCp_2Cl_2$)[30,31] (Fig. 1a). Here, we utilized 4,4'-(anthracene-9,10-diylbis(ethyne-2,1-diyl)dibenzene carboxylic acid (H_2L) as the ligand, featuring alternating aromatic rings and alkyne groups (Fig. 1b). Upon crystallization, a capsule-like MOC, $\{[Cp_3Zr_3(\mu_3\text{-}O)(\mu_2\text{-}OH)_3]_2L_3\}^{2+}$ ($(Cp_3Zr_3)_2L_3$-MOC) crystallizes with Cl^- counterions. Crystallization below 30 °C yields red block-shaped crystals $\{[Cp_3Zr_3(\mu_3\text{-}O)(\mu_2\text{-}OH)_3]_2L_3\}Cl_2$, referred to as **Red-1**, while crystallization above 60 °C result in orange-colored crystals $\{[Cp_3Zr_3(\mu_3\text{-}O)(\mu_2\text{-}OH)_3]_2L_3\}Cl_2$, labeled as **Orange-1**.

Single-crystal X-ray diffraction (SCXRD) revealed that both **Red-1** and **Orange-1** crystallize in the $P\bar{1}$ space group, with comparable cell volumes (Supplementary Table 1). Each structure is composed of $(Cp_3Zr_3)_2L_3$-MOCs (Fig. 1c), consisting of two $\{Cp_3Zr_3(\mu_3\text{-}O)(\mu_2\text{-}OH)_3\}$ nodes linked by three 4,4'-(anthracene-9,10-diylbis(ethyne-2,1-diyl)dibenzene carboxylate) ligands (L) (Fig. 1b, d). X-ray Photoelectron Spectroscopy (XPS) analysis confirms that the oxidation state of Zr is tetravalent (Supplementary Fig. 1) in both compounds. Within the $(Cp_3Zr_3)_2L_3$-MOC, two of the three L ligands have their aromatic groups almost parallel to each other, while the aromatic ring of the third ligand oriented at an angle to the other ligands. Two $(Cp_3Zr_3)_2L_3$-MOCs further stack to form dimers (Fig. 1e, h), which assemble into the overall structure (Fig. 1f, i). By dissolving **Red-1** and **Orange-1** in methanol, we confirm that the same $(Cp_3Zr_3)_2L_3$-MOCs are the major species in both solutions by high resolution mass spectroscopy (Fig. 1g, j). These structural and compositional analyses indicate that **Red-1** and **Orange-1** have the same building units.

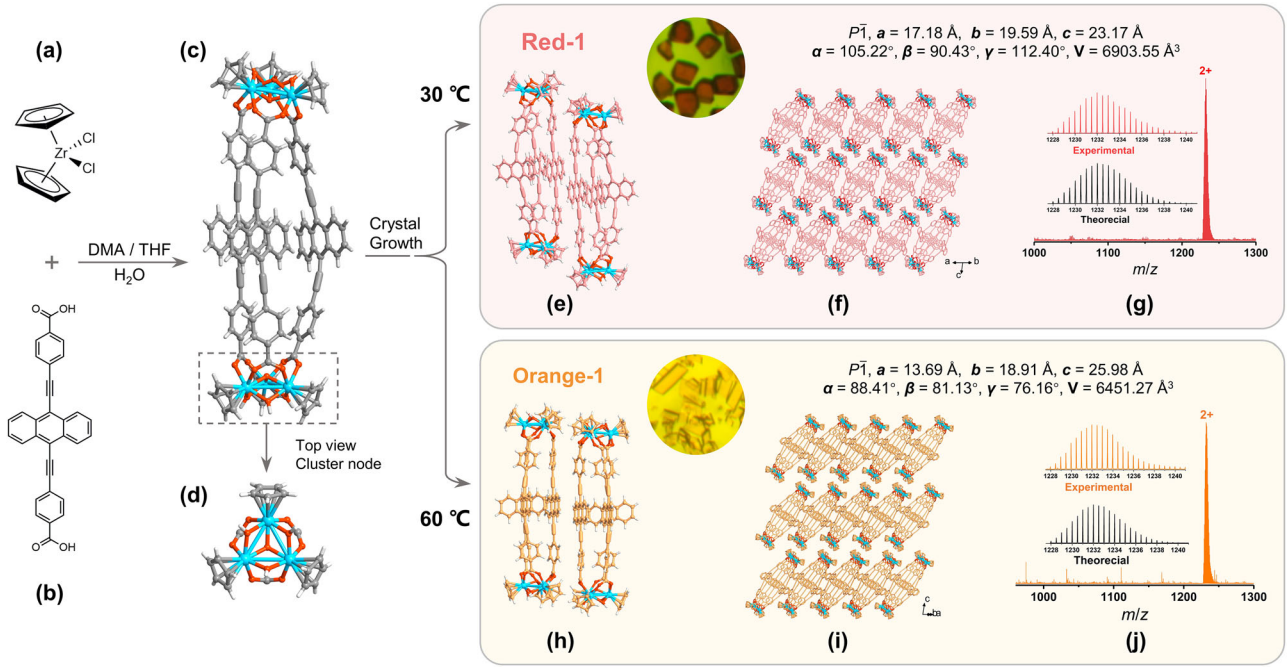

Fig. 1 | The assembly process, structures, and morphologies of Red-1 and Orange-1 crystals. a Chemical structure of the $ZrCp_2Cl_2$. **b** Chemical structure of the ligand H_2L. **c** Chemical structure of the MOCs. Zr, blue sphere; O, red sphere; C, gray sphere; H, light gray sphere. Counterions (Cl^-) and solvent molecules are omitted for clarity. **d** Top view of the cluster node. **e**–**g** the $(Cp_3Zr_3)_2L_3$-MOC dimer structure, lattice packing, and high-resolution electrospray ionization mass spectrum of **Red-1**. The mass spectrum peak of 1,231.9768 corresponds to $[M - 2Cl]^{2+}$ (M = $\{[Cp_3Zr_3(\mu_3\text{-}O)(\mu_2\text{-}OH)_3]_2L_3\}Cl_2$, **Red-1**), exptl m/z = 1,231.9768; calcd m/z = 1,231.9949. **h**–**j** the MOC dimer structure, lattice packing, and high-resolution electrospray ionization mass spectrum of **Orange-1**. The mass spectrum peak at 1,231.9740 correspond to $[M - 2Cl]^{2+}$ (**Orange-1**), exptl m/z = 1,231.9740; calcd m/z = 1,231.9949.

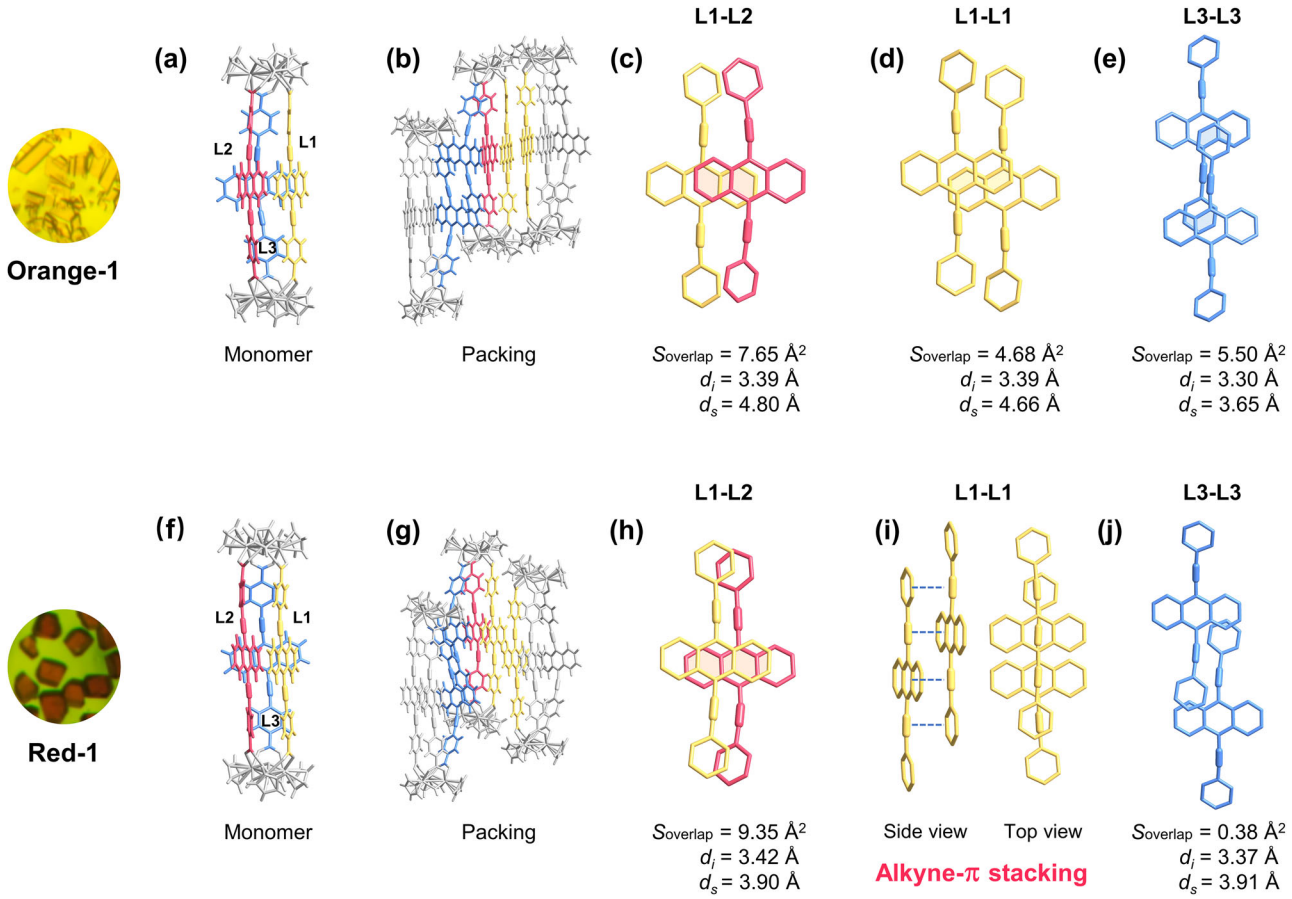

Fig. 2 | Molecular geometric analysis of intra-cage and inter-cage packing in Orange-1 and Red-1, listing the interplanar distance (d_i), π slipping distance (d_s), and π-overlap area ($S_{overlap}$) of aromatic rings. a, **b** the monomer and their stacked structures in **Orange-1**. **c** π-π stacking of L1-L2 in **Orange-1** cage monomers. **d** π-π stacking of L1-L1 in the **Orange-1** dimer. **e** the stacking of L3-L3 between dimers in **Orange-1**. **f**–**h** the monomer and their stacked structures in **Red-1**. **h** π-π stacking of L1-L2 in **Red-1** cage monomers. **i** π-π stacking of L1-L1 in the **Red-1** dimer. **j** the stacking of L3-L3 between dimers in **Red-1**. Note: Four consecutive alkyne-π stackings are observed between L1 ligands in **(i)**.

Although their building units are the same, **Red-1** and **Orange-1** intriguingly show different colors. The differences are likely caused by variations in packing and intermolecular interactions. A close examination of the $(Cp_3Zr_3)_2L_3$-MOC dimers reveals that each $(Cp_3Zr_3)_2L_3$-MOC interacts with its neighbor primarily through ligand-ligand interactions (Fig. 2b, g). In each $(Cp_3Zr_3)_2L_3$-MOC, the three L ligands are crystallographically distinct (color-coded in Fig. 2: L1-yellow, L2-rose red, and L3-blue) (Fig. 2a, f). L1 and L2 are parallel to each other, while L3 forms a certain angle with both L1 and L2. Because an initial analysis of the angles and distances between these ligands within the molecular cage does not immediately clarify their interactions (Supplementary Figs. 2, 3 and Supplementary Table 2), we proceed with a detailed geometric analysis[32]. We gain a deeper understanding of π-π interactions by quantifying the interplanar distance (d_i), π slipping distance (d_s), and π-overlap area ($S_{overlap}$). For the definitions of these three parameters, please refer to S2.4 of the Supplementary Information. The analysis process consists of three steps:

First, the $(Cp_3Zr_3)_2L_3$-MOC monomers of **Red-1** and **Orange-1** exhibit similar structural characteristics. L1 and L2 appear to interact through offset stacked π-π interactions, while L3 interacts with L1 and L2 via edge-to-face stacking. However, our study focuses on analyzing face-to-face stacking and offset stacking interactions. Therefore, the d_i and $S_{overlap}$ between L1 and L2 are 3.39 Å and 7.65 Å², for **Orange-1** (Fig. 2c and Supplementary Fig. 4), and the corresponding values for **Red-1** are 3.42 Å and 9.35 Å² (Fig. 2h).

Second, the two $(Cp_3Zr_3)_2L_3$-MOCs monomers of **Red-1** and **Orange-1** form dimers through L1-L1 interactions. In **Orange-1**, the two L1 ligands form π-π interactions, with the d_i and $S_{overlap}$ being 3.39 Å and 4.68 Å², respectively (Fig. 2d). In contrast, there is no significant overlap between the aromatic rings of L1 ligands in **Red-1** (Fig. 2i), even though they are separated by a similar distance of 3.40 Å as in **Orange-1**.

Third, the stacking arrangement between the dimers of **Red-1** and **Orange-1** is different. In **Orange-1**, the dimers form π-π interactions with the neighboring ones via the aromatic rings on L3 ligands, with the d_i and $S_{overlap}$ being 3.30 Å and 5.50 Å², respectively (Fig. 2e). Conversely, in **Red-1**, the d_i and $S_{overlap}$ between the two L3 ligands are 3.37 Å and 0.38 Å², respectively (Fig. 2j), indicating much weaker π-π slip-stacking interactions.

The above assessments suggest that **Orange-1** exhibits stronger π-π interactions than **Red-1**. Specifically, the intra-dimer and inter-dimer $S_{overlap}$ values of **Orange-1** are 19.98 (7.65 × 2 + 4.68) and 5.50 Å², larger than the corresponding $S_{overlap}$ (18.70 (9.35 × 2) Å² and 0.38 Å²) of **Red-1**. It is well-known that molecular packings involving more effective π-π interactions often lead to a more significant red-shift in light absorption and emission[32,33]. However, **Red-1**, with overall less π-π interactions, exhibits a more red-shifted color in appearance. Such a puzzle raises the possibility that other interactions may contribute to the color of the crystals.

Validation of the alkyne-π stacking interactions

After further examining the ligand interactions (Fig. 2i), we find an intriguing pattern of intra-dimer interactions in **Red-1**. Particularly, the two neighboring L1 ligands are nearly parallel, with the dihedral angle smaller than 1.1° and the distance within 3.50 Å (Supplementary Fig. 5). Besides, the alkyne in one L1 ligand stacks with the aromatic rings in the other L1 ligand,

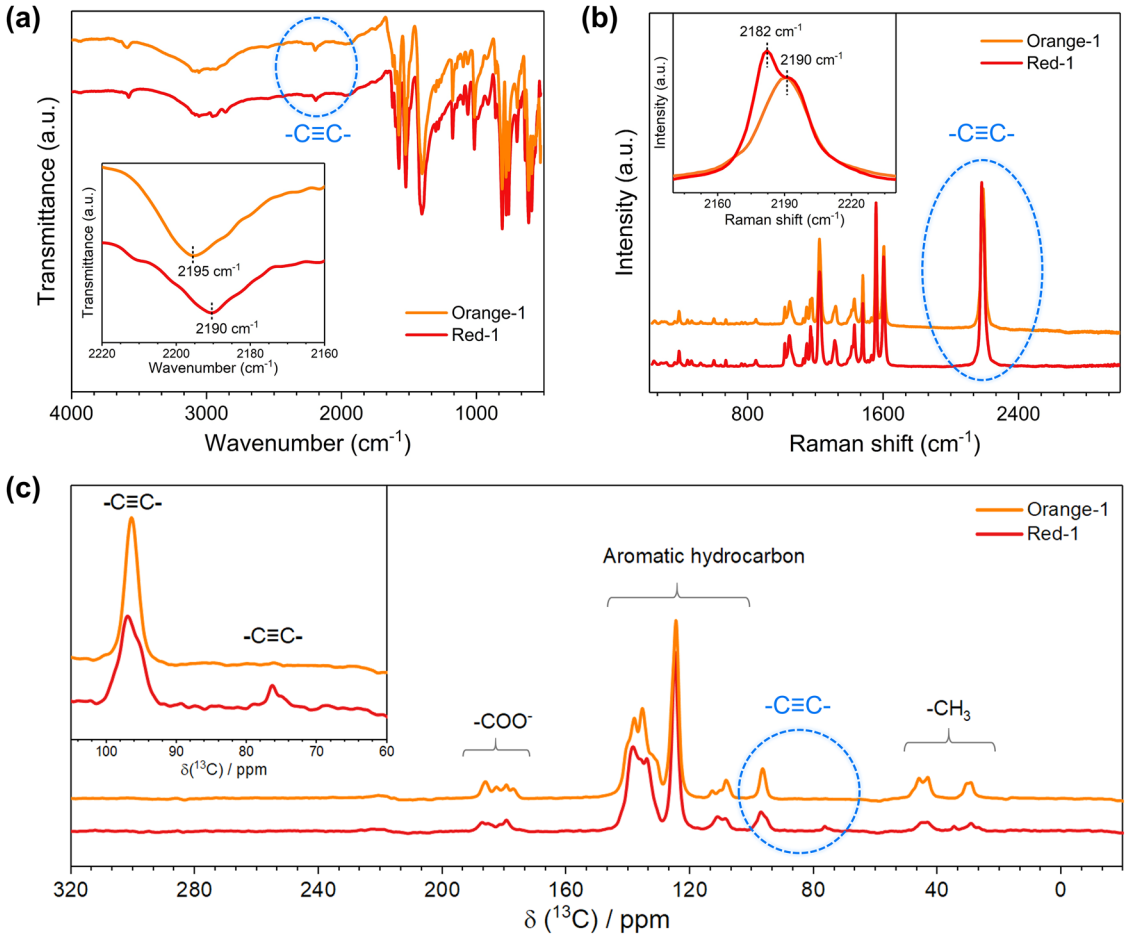

Fig. 3 | Spectroscopic verification of alkyne-π interactions. a Fourier Transform Infrared (FTIR) spectroscopy. The inset shows the vibrational signals of the C≡C bonds. **b** Raman spectroscopy. The inset shows the vibrational signals of the C≡C bonds. The C≡C stretching signal of the **Red-1** crystal is composed of two components, one matching **Orange-1** and one not. **c** ^{13}C Solid-State Nuclear Magnetic Resonance spectroscopy. The inset provides a magnified view of the C≡C bond region (60-100 ppm). The C≡C signals of the **Red-1** crystal are composed of two components.

and four pairs of such alkyne-aromatic-ring stackings occur consecutively between the two L1 ligands. By sharp contrast, the alkyne-alkyne and alkyne-aromatic-ring distances in **Orange-1** all exceed 4.60 Å (Supplementary Fig. 6), beyond the typical range for considering intermolecular interactions[34]. Although crystal packing factors like symmetry and solvent molecules may influence these molecular arrangements, the stacking patterns of **Red-1** and **Orange-1** are distinctly different. We thus propose that unique interactions between the alkyne and aromatic rings in **Red-1** contribute to its counterintuitive red-shifted color.

To examine the existence of such alkyne-π interactions, we performed comprehensive spectroscopic studies on the C≡C bonds in both **Red-1** and **Orange-1** using phase-pure polycrystalline powders (XRD patterns in Supplementary Fig. 7). Fourier Transform Infrared (FTIR) spectroscopy (Fig. 3a and Supplementary Fig. 8a) reveals a characteristic C≡C stretching signal at 2195 cm^{-1} for **Orange-1**. For **Red-1**, the corresponding signal is red-shifted to 2190 cm^{-1}, indicating that the C≡C bonds in **Red-1** are indeed distinct. Given the intrinsic weakness of the C≡C stretching signal in FTIR spectra[35], we also characterized the samples using Raman spectroscopy (Fig. 3b and Supplementary Fig. 8b). Importantly, we observed a unique C≡C stretching signal at 2182 cm^{-1} for **Red-1**, clearly red-shifted from the normal C≡C stretching peak at 2190 cm^{-1} in both samples. This interesting observation suggests that a portion of C≡C bonds are influenced by interactions only present in **Red-1**, i.e., those stacked with the aromatic rings. The red-shifted signals in FTIR and Raman spectra provide direct evidence to support the existence of alkyne-π interactions[36,37].

We further characterize the chemical environment of the C≡C bonds by ^{13}C Solid-State Nuclear Magnetic Resonance (^{13}C SSNMR). Although the signals in the ^{13}C SSNMR spectra are relatively broad, they are distinguishable for identifying different carbon atoms (Fig. 3c and Supplementary Fig. 8c). **Red-1** and **Orange-1** both exhibit clear signals corresponding to the carboxylate groups (170.0 to 190.0 ppm) and the aromatic rings (100.0 to 150.0 ppm). In the alkyne region (60.0 to 100.0 ppm), **Orange-1** exhibits only one broad peak at 96.0 ppm, corresponding to the alkyne groups that are not involved in intermolecular interactions. **Red-1**, on the other hand, exhibits two peaks at 97.0 ppm and 76.0 ppm. The upfield signal at 76.0 ppm results from the shielding effect of the aromatic ring current[38], confirming the alkyne groups are involved in the alkyne-π stacking interactions. These findings align well with the FTIR and Raman spectroscopic results, lending credence to the assertion that the alkyne-π interaction is a true intermolecular interaction.

Effect of alkyne-π interactions

Having confirmed the presence of alkyne-π stacking interactions, we proceed to investigate their influence from three key aspects, including energy analysis, vibrational spectroscopy, and light absorption/emissions.

Computational analysis on the energetics. To estimate the energy contributions from alkyne-π interactions, we conduct a detailed analysis of the interaction energies within the dimers, mainly focusing on the seven pairs of π-π and alkyne-π interactions between the adjacent L1 ligands as depicted in Fig. 4a (for the computational details, please refer to

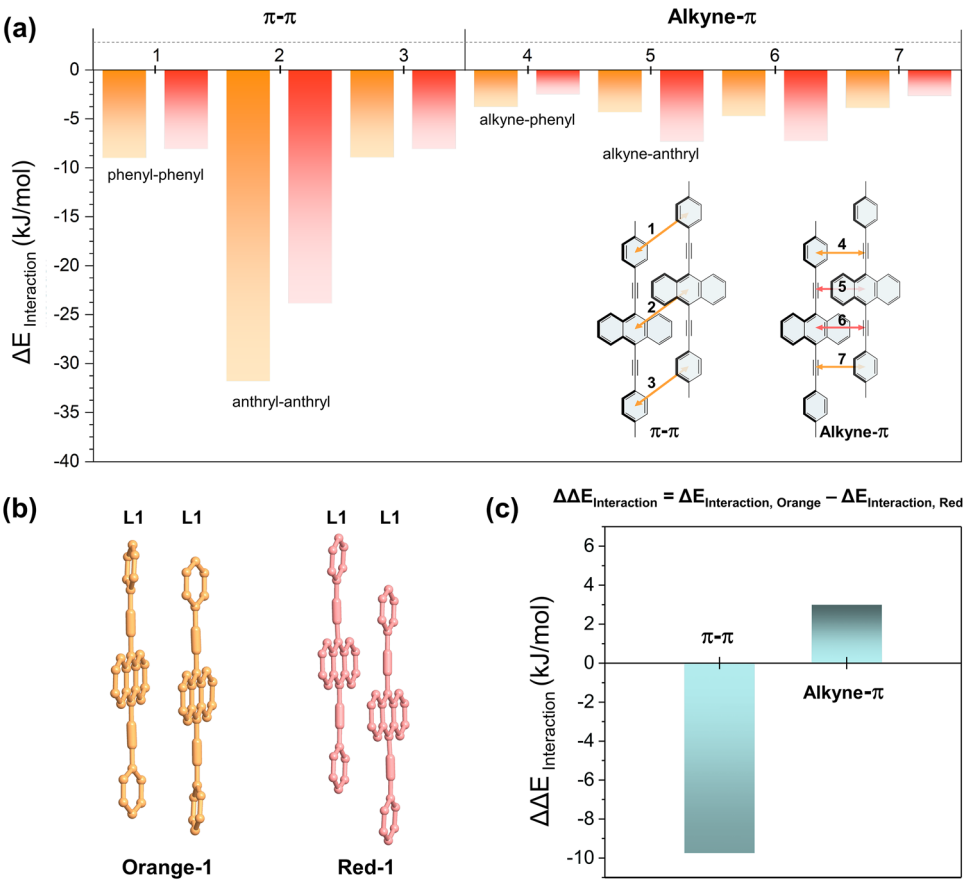

Fig. 4 | Energy calculations provide critical insights into the energy contribution of π-π and alkyne-π interactions. a Calculations of the π-π and alkyne-π interactions between the adjacent L1 ligands in dimeric units. Seven pairs of interactions are numbered as shown in the inset and their energy values are plotted accordingly (Numbers 1 and 3 represent the π–π interactions between benzene rings; number 2 represents the π–π interactions between anthracene rings; numbers 4 and 7 represent the alkyne–π interactions between alkyne groups and benzene rings; numbers 5 and 6 represent the alkyne–π interactions between alkyne groups and anthracene rings). **b** Diagram showing the relative positions and orientations of two L1 ligands in **Red-1** and **Orange-1** dimers. **c** Variations of π-π and alkyne-π interaction energies from **Orange-1** to **Red-1** dimer.

the Supplementary Information and Supplementary Data 1). Notably, although the relative positions and orientations of two L1 ligands in the **Orange-1** and **Red-1** dimers are different (Fig. 4b), the π-π interactions are consistently observed to be more robust than their alkyne-π counterparts (Supplementary Figs. 9 and 10). However, a discernible difference emerges when we closely examine the relative strength of these interactions in each dimer. To quantify these variations, we calculated $\Delta\Delta E_{Interaction}$, defined as the interaction energy between the two L1 ligands in **Orange-1** minus that in **Red-1** (Fig. 4c). In this definition, a positive $\Delta\Delta E_{Interaction}$ value indicates that the interaction is stronger in **Red-1**, whereas a negative value indicates a stronger interaction in **Orange-1**. Based on this metric (Supplementary Table 3), our results show that π-π interactions contributed by anthracene-anthracene and phenyl-phenyl interactions in the **Orange-1** dimer are stronger than those in the **Red-1** dimer (Fig. 4c). On the contrary, the alkyne-π interactions consisting of alkyne-phenyl and alkyne-anthracene interactions in the **Red-1** dimer are stronger than in the **Orange-1** dimer (Fig. 4c). Therefore, transitioning from the **Orange-1** dimer to the **Red-1** dimer, the predominant alterations in the intra-dimer interactions involve a reduction in π-π interactions and a concomitant enhancement of alkyne-π interactions. Hence, our analysis reveals that, although alkyne-π interactions are energetically less significant compared to π-π interactions, they elaborate the main difference in the intra-dimer interactions in the **Red-1** dimer relative to the **Orange-1** dimer.

Spectrum-changing: Part 1 - On vibrational spectroscopy. Alkyne-π interaction clearly has an effect on vibration spectroscopies. In Section 2, we showed that the C≡C stretching signal in **Red-1** shifts to lower wavenumbers in both FTIR and Raman spectra. The red-shift, observed within a range of 10 cm^{-1}, suggests a minor reduction in the C≡C bond strength. As we know, the red-shifting vibrational signals have been extensively studied in the context of "back-bonding" from transition metals to CO molecules in carbonyl complexes[39]. Similar behaviors have been observed in the C≡N vibrational signal when interacting with the Ag nanoparticles in a "side-on" configuration[40]. Therefore, the red-shifted C≡C vibration signal in **Red-1** is likely caused by the donation of π electrons from aromatic rings to the anti-bonding orbitals of the alkynes, which is a direct consequence of the alkyne-π interaction.

Spectrum-changing: Part 2 - on light absorption and emission. Finally, the change in light absorption and emission naturally falls within our interest. The UV-Vis spectra of the crystalline powders of the two compounds show different absorption ranges. For **Orange-1**, absorption takes place from 200 nm to 580 nm, while **Red-1** absorbs from 200 nm to 620 nm. In the visible region, the absorption edge of **Red-1** is clearly red-shifted from that of **Orange-1** (Fig. 5a), leading to their color differences. We use the Tauc plot to determine the bandgap from UV-Vis data[41]. The fitting of $(\alpha h\nu)^{1/n} = B(h\nu - E_g)$ indicates that $n = 2$, confirming that both materials are direct bandgap semiconductors. Specifically, **Orange-1** exhibits a bandgap of 2.14 eV, whereas **Red-1** has a bandgap of 2.09 eV, with a difference of 0.05 eV (Supplementary Fig. 11). This variation is mainly attributed to the alkyne-π interactions in **Red-1**, which cause a reduction in the optical bandgap and a red shift in the absorption spectrum. Meanwhile, we find that the methanol solution of **Red-1** and **Orange-1** exhibit high similarity in the UV and luminescent spectra (Fig. 5b) (see discussion in the Supplementary Information and Supplementary Figs. 12–15 and Supplementary Table 4). This suggests that the differences in solid-state stacking structures, in particular the alkyne-π interactions, is likely the primary cause of the absorption red-shift in **Red-1** crystals.

We further studied the fluorescent emission properties of the two compounds. Under 410 nm excitation, **Orange-1** exhibits maximum emission at 600 nm (with a quantum yield PLQY of 0.56%), while the maximum emission peak of **Red-1** is located at 640 nm (PLQY = 8.60%).

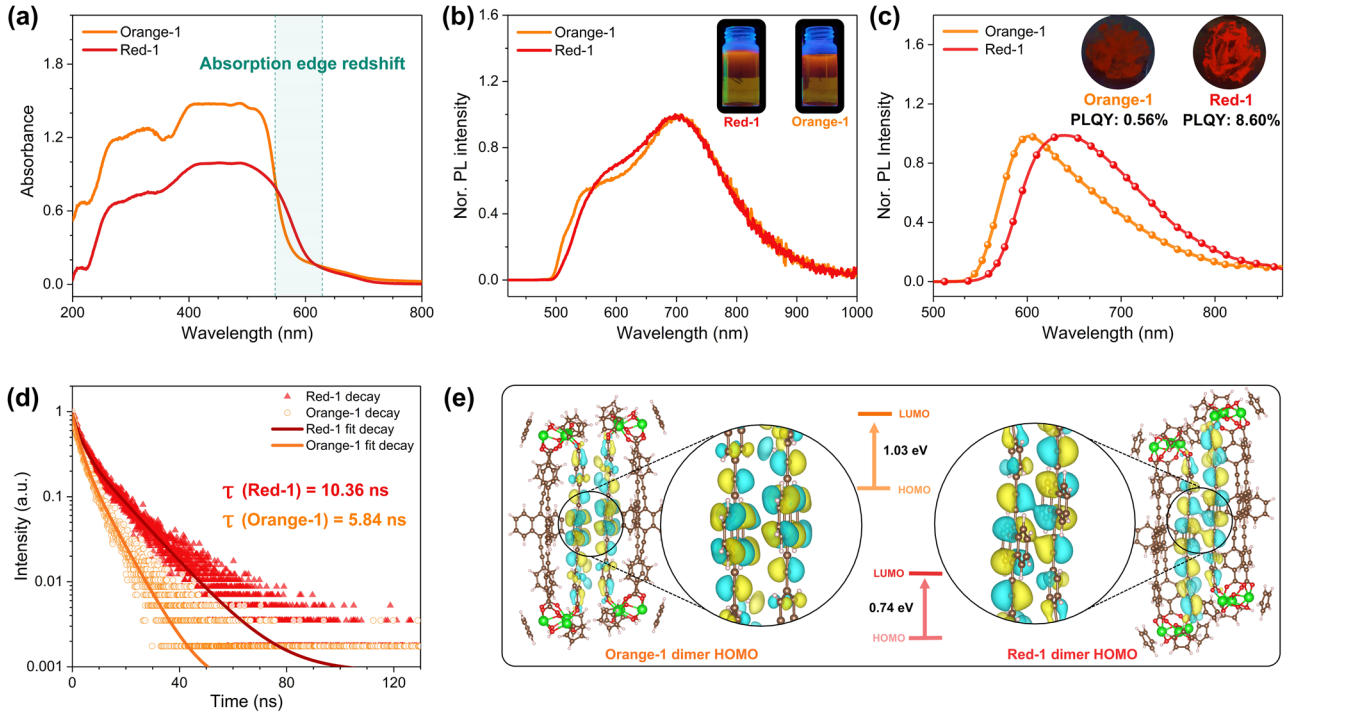

Fig. 5 | Effects of alkyne-π interaction on absorption and emission. a Fluorescence spectrum of the methanol solution of **Red-1**/**Orange-1** (λ_{ex} = 410 nm). The inset shows the appearance of the solutions under 365-nm UV exposure. **b** UV-visible absorption spectra of the polycrystalline powders, indicating the red-shifted absorption edge of **Red-1**. **c** Fluorescence emission spectrum of the polycrystalline powders (λ_{ex} = 410 nm), with a pronounced red-shift in **Red-1**. The inset displays the photographs (under 365-nm UV exposure). **d** Fluorescence lifetime analysis, fitted with a double exponential decay model. **e** Visualization of the highest occupied molecular orbital (HOMO) of **Red-1** and **Orange-1**.

Therefore, the "red-shift" characteristic is again observed in the fluorescent emission of **Red-1**, accompanied by a 15-fold increase in PLQY (Fig. 5c). In addition, time-resolved fluorescence spectra are fitted with a double exponential decay model[42], yielding an average lifetime of 10.36 ns for **Red-1** (Fig. 5d). This fluorescence lifetime is about twice as long as that of **Orange-1** (5.84 ns). With the higher PLQY and longer lifetime, the nonradiative rate (k_{nr} = (1-PLQY)/τ) of **Red-1** is calculated to be 0.088 ns^{-1}, clearly lower than that of **Orange-1** (k_{nr} = 0.38 ns^{-1})[43,44]. As mentioned, increasing π-π overlap typically induces a more pronounced red-shift in the optical properties[32,33,45]. However, despite the more significant π-π interactions in the **Orange-1**, its optical spectra, counterintuitively, exhibit less red-shifting when compared to **Red-1**. Since the primary distinction between **Orange-1** and **Red-1** is identified as a decrease in π-π interactions and a simultaneous strengthening of alkyne-π interactions in the latter, we hypothesize that the alkyne-π interactions may predominantly govern the red-shift in absorption and emission properties observed in **Red-1**.

To verify this conjecture, we investigate the electronic structures of **Orange-1** and **Red-1** in the crystal environment by DFT calculations. First, we find that **Red-1** has a narrower thermal bandgap than **Orange-1**, mainly because the conduction band shifts to a lower energy region (Supplementary Fig. 16 and Supplementary Table 5). In accordance with the bandgap, computations also suggest a smaller HOMO-LUMO gap in **Red-1**. These results are consistent with the UV-Vis data, indicating that our computational models can reproduce the spectral features observed in the experiment. To further decipher the molecular origin of the red-shift observed in the spectra, we examine the orbital distribution of frontier molecular orbitals over the molecular fragments[46]. We focus on the regions of L1 ligands, as they are essential for determining the interactions between $(Cp_3Zr_3)_2L_3$-MOCs. Interestingly, the HOMOs of **Red-1** and **Orange-1** show clear discrepancies. In particular, in **Red-1**, alkyne groups in the L1 ligand on one monomer appear to form "bonding interactions" with the anthracene rings of the L1 ligand on the other monomer (Fig. 5e). However, such interactions are not observed in **Orange-1**. This discrepancy between the HOMOs of **Red-1** and **Orange-1** helps us rationalize the smaller HOMO-LUMO gap in **Red-1** and offers molecular insights into the red-shift observed in the spectra.

It is worth noting that the effect of alkyne-π interactions on light absorption/emission can be extended to other phases beyond **Red-1**. Particularly, by controlling the synthetic temperature at 0 °C, a new phase (**Red-2**) is successfully obtained (Supplementary Fig. 17a). Meanwhile, by dissolving **Red-1** in methanol followed by evaporation, we obtain another new compound with orange color (**Orange-2**) (Supplementary Fig. 17b, c). The detailed analyses of the intermolecular interactions in **Red-2** and **Orange-2** are shown in the Supplementary Discussions and Supplementary Figs. 18 and 19. Interestingly, alkyne-π stacking interactions are also observed in **Red-2** but not in **Orange-2**. These observations further corroborate the significant influence of the alkyne-π interactions on light absorption and emission.

Exploring the broader impacts of alkyne-π interaction

Upon discovering the existence of alkyne-π stacking interaction in our newly prepared functional materials, we conducted a structural search in the Cambridge Crystallographic Data Centre (CCDC). Three parameters are defined for this analysis: α is the angle between the C≡C bond axis and the ring normal; θ represents the angle between the ring normal and a vector connecting the C≡C bond center and the ring center; and d is the distance between the C≡C bond center and the ring center (Fig. 6a). As illustrated in the heatmap (Fig. 6b), C≡C bonds predominantly orient parallel to the aromatic ring (with $\alpha \sim 90°$, perpendicular to the ring normal). After zooming in, two hotspots are identified, one at ~3.5 Å and the other at ~5.0 Å (Fig. 6c). By plotting these hits against θ (Fig. 6d), we observe that the 3.5 Å hotspot remains at θ near 0°. This 3.5 Å hotspot closely aligns with the alkyne-π stacking interaction we described here, representing a total of 436 structures (Supplementary Figs. 20a, 20b, Supplementary Table 6, and Supplementary Data 2), e.g., **MEFREX**[47] and **CIMKOB**[48] (Fig. 6e and Supplementary Figs. 21, 22). On the other hand, the 4.3 Å hotspot in Fig. 6d,

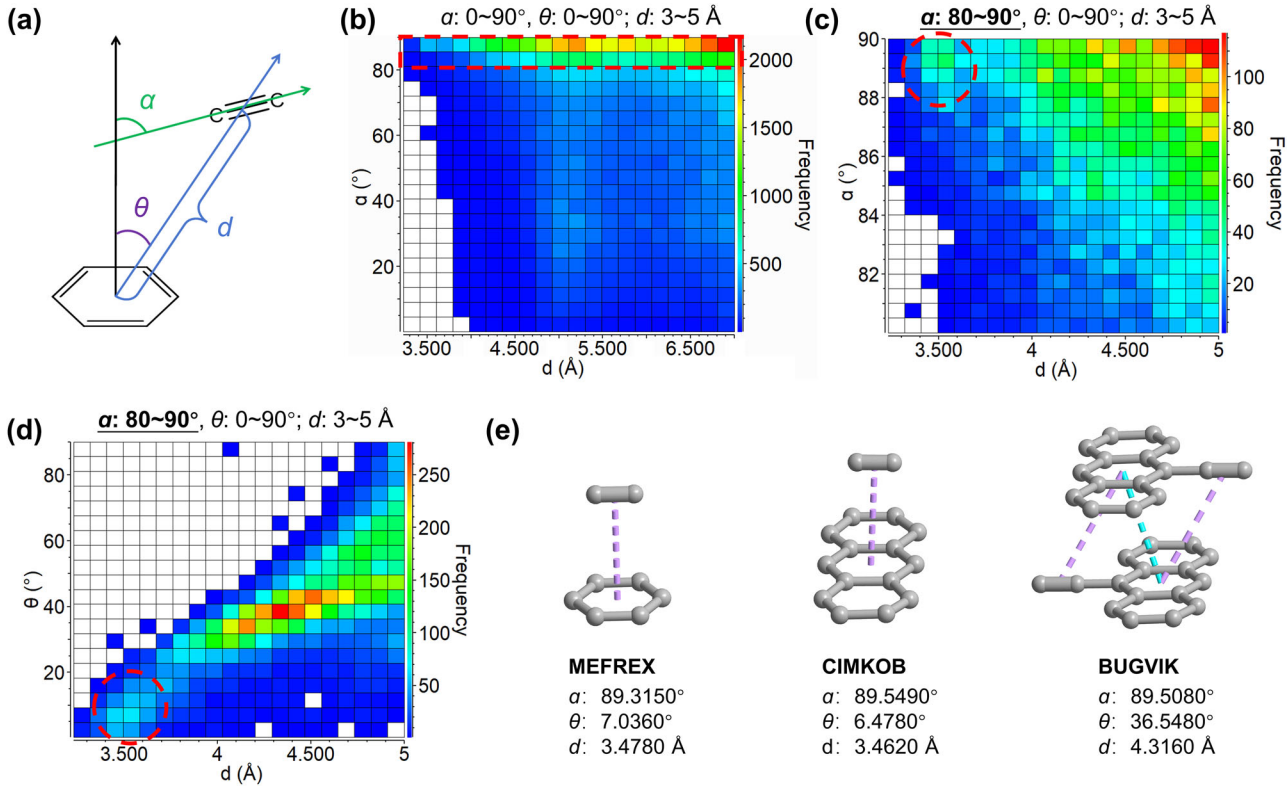

Fig. 6 | Exploration of alkyne-π stacking interactions using the Cambridge Crystallographic Data Centre. a Three parameters, α, θ, and d, are defined for data retrieval and analysis. **b** Heat map (α 0°~90°; θ 0°~90°; d 3~5 Å) with hotspots near α at 90°. **c** Heat map with α restricted to 80°~90°, showing hotspots located at ~3.5 Å and ~5.0 Å. **d** Heat map relating d with θ (α = 80°~90°), showing the hotspot at 3.5 Å persists (highlighted by the red dashed line). This demonstrates the alkyne-π stacking as a characteristic interaction pattern. **e MEFREX** and **CIMKOB** represent structures from the 3.5 Å hotspot in (**d**), while **BUGVIK** represents a structure from the 4.3 Å hotspot.

including a total of 1704 structures (Supplementary Figs. 20c, 20d, Supplementary Table 7, and Supplementary Data 2), e.g., **BUGVIK**[49] (Fig. 6e and Supplementary Fig. 23), are attributed to the parasitic stacking geometry caused by slip-stacking π-π interactions, which out-compete the alkyne-π interactions. These findings unveil the alkyne-π stacking as a subtle but characteristic interaction mode.

Regarding the "spectrum changing" effect, alkyne-π interactions may affect the resolution of alkyne-tagged probes during bio-imaging. In particular, previous researchers have reported a series of alkyne-tagged imaging probes (i.e., Carbow)[28], with the C≡C vibration signals differing by only 5 cm^{-1}. The "high resolution" of alkyne-tagged probes could be diminished by alkyne-π interactions, because we found that alkyne-π interactions could lead to a red-shift of the Raman signal up to ~10 cm^{-1} (Fig. 3b). Therefore, caution is needed when applying alkyne-tagged probes in complex biological systems, where the probes might undergo substantial alkyne-π interactions with biomolecules.

Furthermore, we notice a recent report on the successful synthesis of polyyne polyrotaxanes with multiple threaded macrocycles[50]. For unthreaded polyynes, the C≡C stretching signals are observed at 1944 cm^{-1} (compound **C28**) (Supplementary Fig. 24a) and 1913 cm^{-1} (compound **C48**) (Supplementary Fig. 25a). After threading through the macrocycles, the corresponding signals red-shift to 1940/1940 cm^{-1} (compound **C28**·$(M_a)_2$/ **C28**·$(M_b)_2$) (Supplementary Fig. 24b) and 1909/1907 cm^{-1} (compound **C48**·$(M_a)_3$/ **C48**·$(M_b)_3$) (Supplementary Fig. 25b). Based on the single crystal structure of similar compounds reported by the same paper (Supplementary Fig. 26), we speculate that this red-shift might be caused by alkyne-π stacking. Therefore, the red-shifted C≡C Raman signal could serve as a signature of the successful synthesis of polyyne-threaded macrocycles.

Finally, it is worth noting that although the existence of alkyne-π interaction is evident in the solid state, we haven't found a solvent that seems to maintain the alkyne-π interaction. Therefore, the presence of this interaction in the solid state might not guarantee its persistence after entering the solution. We are currently still exploring the right solvent that might maintain this intermolecular interaction.

Conclusion

In summary, we systemically analyze two zirconocene metal-organic cage compounds and unveil the existence of alkyne-π interactions. The stacking of alkyne groups directly above aromatic rings is recognized as the unique structural feature, with spectroscopic studies indicating the changing C≡C bond characters because of the alkyne-π interactions. Despite being energetically less potent than π-π interactions, alkyne-π interactions significantly influence the spectroscopic properties of the compounds, as evidenced by red-shifting effects observed across vibrational, absorption, and emission spectra. Together, our findings reveal the role of alkyne-π interactions in modulating the spectroscopic properties with functional relevance. This research expands our understanding of intermolecular forces and highlights the role of alkyne-π interactions in developing functional materials for advanced applications in chemistry and biology. It also underscores the importance of considering subtle yet impactful interactions in the development of supramolecular chemistry.

Methods

Starting materials

All reagents, including bis(cyclopentadienyl)zirconium dichloride and 4,4'-(anthracene-9,10-diylbis(ethyne-2,1-diyl))dibenzoic acid used in this study, were purchased from Shanghai Bide Pharmatech Co., Ltd. and used without further purification. All solvents were obtained from Sinopharm Chemical Reagent Co., Ltd. and used directly without additional purification.

Synthesis of $\{[Cp_3Zr_3(\mu_3\text{-}O)(\mu_2\text{-}OH)_3]_2L_3\}Cl_2$ (Cp = η_5-C_5H_5) (Red-1)

Bis(cyclopentadienyl)zirconium dichloride ($ZrCp_2Cl_2$, where Cp = η^5-C_5H_5) (32.6 mg, 0.112 mmol) and 4,4-(anthracene-9,10-diylbis(e-thyne-2,1-diyl))dibenzoic acid (H_2L) (4.1 mg, 0.00879 mmol) were dissolved in DMA/THF mixed solvent (2.0 mL, v/v = 1/1). Shake to dissolve and add distilled water (190 μL). The mixture was ultrasonicated at 0 °C for 30 minutes followed by volatilization at 30 °C to obtain red crystals (**Red-1**). Yield: 59% (based on Zr). IR (2000-400 cm^{-1}): 3578 (w), 2190 (w), 1576 (m), 1523 (m), 1406 (s), 1176 (s), 1064 (w), 1016 (m), 809 (s), 778 (s), 761 (s), 614 (s), 591 (m). HRMS (*m*/*z*): $[M-2Cl]^{2+}$ (M = $\{[Cp_3Zr_3(\mu_3\text{-}O)(\mu_2\text{-}OH)_3]_2L_3\}Cl_2$), found *m*/*z* = 1231.9768; calculated *m*/*z* = 1231.9949. ^{1}H NMR spectrum for **Red-1** (500 MHz, CD_3OD) δ6.57-6.63 (s, 10H), 6.64-6.69 (m, 4H), 7.42-7.48 (d, 4H), 7.71-7.76 (d, 4H), 7.97-8.01 (m, 4H).

Synthesis of $\{[Cp_3Zr_3(\mu_3\text{-}O)(\mu_2\text{-}OH)_3]_2L_3\}Cl_2$ (Cp = η_5-C_5H_5) (Orange-1)

Bis(cyclopentadienyl)zirconium dichloride ($ZrCp_2Cl_2$, where Cp = η^5-C_5H_5) (32.6 mg, 0.112 mmol) and 4,4-(anthracene-9,10-diylbis(e-thyne-2,1-diyl))dibenzoic acid (H_2L) (4.1 mg, 0.00879 mmol) were dissolved in DMA/THF mixed solvent (2.0 mL, v/v = 1/1). Shake to dissolve and add distilled water (190 μL). The mixture was ultrasonicated at 0 °C for 30 minutes followed by volatilization at 60 °C to obtain orange crystals (**Orange-1**). Yield: 68% (based on Zr). IR (2000–400 cm^{-1}): 3586 (w), 2195 (w), 1576 (m), 1523 (m), 1404 (s), 1176 (s), 1066 (w), 1016 (m), 809 (s), 778 (s), 761 (s), 614 (s), 591 (m). HRMS (*m*/*z*): $[M-2Cl]^{2+}$ (M = $\{[Cp_3Zr_3(\mu_3\text{-}O)(\mu_2\text{-}OH)_3]_2L_3\}Cl_2$), found *m*/*z* = 1231.9740; calculated *m*/*z* = 1231.9949. ^{1}H NMR spectrum for **Orange-1** (500 MHz, CD_3OD) δ6.56–6.63 (s, 10H), 6.63-6.69 (m, 4H), 7.43-7.48 (d, 4H), 7.71-7.76 (d, 4H), 7.96-8.02 (m, 4H).

Synthesis of $\{[Cp_3Zr_3(\mu_3\text{-}O)(\mu_2\text{-}OH)_3]_2L_3\}Cl_2$ (Cp = η_5-C_5H_5) (Red-2)

The synthesis of the reaction mixture is identical to that of **Red-1**. The reaction mixture is subjected to ultrasonic treatment at 0 °C for 30 minutes, followed by evaporation at 0 °C to obtain red block-shaped crystals (**Red-2**).

Synthesis of $\{[Cp_3Zr_3(\mu_3\text{-}O)(\mu_2\text{-}OH)_3]_2L_3\}Cl_2$ (Cp = η_5-C_5H_5) (Orange-2)

Dissolve the dry **Red-1** crystals (10.0 mg) in methanol (50.0 mL), noting that the crystals are only slightly soluble. After filtering and sealing the solution, let it stand at room temperature to slowly evaporate over 3 months, yielding orange rhombic crystals (**Orange-2**).

Data availability

The data supporting the results presented in this study are available from the corresponding author upon reasonable request. The X-ray crystallographic coordinates for the structures reported herein have been deposited with the Cambridge Crystallographic Data Centre (CCDC), with the deposition numbers CCDC 2337732-2337735. This information may be obtained without charge from http://www.ccdc.cam.ac.uk/data_request/cif. All other data relevant to this study are available from the authors upon reasonable request.

Received: 20 May 2025; Accepted: 3 November 2025;
Published online: 12 December 2025

References

1. Riley, K. E. & Hobza, P. Noncovalent interactions in biochemistry. *Wiley Interdiscip. Rev.:Comput. Mol. Sci.* **1**, 3–17 (2011).
2. Martinez, C. R. & Iverson, B. L. Rethinking the term “pi-stacking. *Chem. Sci.* **3**, 2191–2101 (2012).
3. Bloom, J. W. G., Raju, R. K. & Wheeler, S. E. Physical nature of substituent effects in XH/π interactions. *J. Chem. Theory Comput.* **8**, 3167–3174 (2012).
4. Nishio, M., Umezawa, Y., Fantini, J., Weiss, M. S. & Chakrabarti, P. CH–π hydrogen bonds in biological macromolecules. *Phys. Chem. Chem. Phys.* **16**, 12648–12683 (2014).
5. Ma, J. C. & Dougherty, D. A. The cation−π interaction. *Chem. Rev.* **97**, 1303–1324 (1997).
6. Kennedy, C. R., Lin, S. & Jacobsen, E. N. The cation–π interaction in small-molecule catalysis. *Angew. Chem., Int. Ed.* **55**, 12596–12624 (2016).
7. Frontera, A., Gamez, P., Mascal, M., Mooibroek, T. J. & Reedijk, J. Putting anion–π interactions into perspective. *Angew. Chem. Int. Ed.* **50**, 9564–9583 (2011).
8. Molina, P., Zapata, F. & Caballero, A. Anion recognition strategies based on combined noncovalent interactions. *Chem. Rev.* **117**, 9907–9972 (2017).
9. Egli, M. & Gessner, R. V. Stereoelectronic effects of deoxyribose O4’ on DNA conformation. *Proc. Natl. Acad. Sci. USA.* **92**, 180–184 (1995).
10. Egli, M. & Sarkhel, S. Lone pair-aromatic interactions: to stabilize or not to stabilize. *Acc. Chem. Res.* **40**, 197–205 (2007).
11. Mooibroek, T. J., Gamez, P. & Reedijk, J. Lone pair–π interactions: a new supramolecular bond? *CrystEngComm* **10**, 1501–1515 (2008).
12. Deng, J.-H. et al. π-π stacking interactions: Non-negligible forces for stabilizing porous supramolecular frameworks. *Sci. Adv.* **6**, eaax9976 (2020).
13. Tang, M. et al. Molecular-strain engineering of double-walled tetrahedra. *Chem*. **7**, 2160–2174 (2021).
14. Münzfeld, L. et al. Synthesis and properties of cyclic sandwich compounds. *Nature* **620**, 92–96 (2023).
15. Li, G.-L. et al. Constructing π-stacked supramolecular cage based hierarchical self-assemblies via π···π stacking and hydrogen bonding. *J. Am. Chem. Soc.* **143**, 10920–10929 (2021).
16. Mazik, M. Molecular recognition of carbohydrates by acyclic receptors employing noncovalent interactions. *Chem. Soc. Rev.* **38**, 935–956 (2009).
17. Neel, A. J., Hilton, M. J., Sigman, M. S. & Toste, F. D. Exploiting non-covalent π interactions for catalyst design. *Nature* **543**, 637–646 (2017).
18. Zahradník, R. Interactions between Ions and molecules: gas-phase theoretical studies. *Acc. Chem. Res.* **28**, 306–312 (1995).
19. CURTISS, L. A. & BLANDER, M. Thermodynamic properties of gas-phase hydrogen-bonded complexes. *Chem. Rev.* **88**, 827–841 (1988).
20. Biswas, S. et al. Universal readers based on hydrogen bonding or π–π stacking for identification of DNA nucleotides in electron tunnel junctions. *ACS Nano* **10**, 11304–11316 (2016).
21. Cotelle, Y., Lebrun, V., Sakai, N., Ward, T. R. & Matile, S. Anion-π enzymes. *ACS Cent. Sci.* **2**, 388–393 (2016).
22. Craven, T. W., Cho, M.-K., Traaseth, N. J., Bonneau, R. & Kirshenbaum, K. A miniature protein stabilized by a cation−π interaction network. *J. Am. Chem. Soc.* **138**, 1543–1550 (2016).
23. Yamakoshi, H. et al. Alkyne-Tag Raman imaging for visualization of mobile small molecules in live cells. *J. Am. Chem. Soc.* **134**, 20681–20689 (2012).
24. Ponzini, F., Zagha, R., Hardcastle, K. & Siegel, J. S. Phenyl/Pentafluorophenyl interactions and the generation of ordered mixed crystals:sym-Triphenethynylbenzene and sym-Tris (perfluorophenethynyl)benzene. *Angew. Chem.* **112**, 2413–2415 (2000).
25. Kissel, P. et al. A two-dimensional polymer prepared by organic synthesis. *Nat. Chem.* **4**, 287–291 (2012).
26. Dodo, K., Fujita, K. & Sodeoka, M. Raman Spectroscopy for chemical biology research. *J. Am. Chem. Soc.* **144**, 19651–19667 (2022).
27. Koike, K. et al. Quantitative drug dynamics visualized by alkyne-tagged plasmonic-enhanced Raman Microscopy. *ACS Nano* **14**, 15032–15041 (2020).
28. Hu, F. et al. Supermultiplexed optical imaging and barcoding with engineered polyynes. *Nat. Methods* **15**, 194–200 (2018).

29. Li, J. J. & Yang, M. Chapter 1: Alkynes, *Drug Discovery with Privileged Building Blocks: Tactics in Medicinal Chemistry* (eds. Li, J. J. & Yang, M.) 1-14 (CRC Press, 2022).
30. Liu, G., Ju, Z., Yuan, D. & Hong, M. In situ construction of a coordination Zirconocene Tetrahedron. *Inorg. Chem.* **52**, 13815–13817 (2013).
31. El-Sayed, E.-S. M., Yuan, Y. D., Zhao, D. & Yuan, D. Zirconium metal–organic cages: synthesis and applications. *Acc. Chem. Res.* **55**, 1546–1560 (2022).
32. Dharmarwardana, M. et al. Strong π-stacking causes unusually large anisotropic thermal expansion and thermochromism. *Proc. Natl. Acad. Sci.* **118**, e2106572118 (2021).
33. Zhang, H. Y., Zhang, Z. L., Ye, K. Q., Zhang, J. Y. & Wang, Y. Organic crystals with tunable emission colors based on a single organic molecule and different molecular packing structures. *Adv. Mater.* **18**, 2369–2372 (2006).
34. Janiak, C. A critical account on π–π stacking in metal complexes with aromatic nitrogen-containing ligands †. *J. Chem. Soc., Dalton Trans*. **2000**, 3885–3896 (2000).
35. Wu, P. P., HSU, S. L., THOMAS, O. & BLUMSTEIN, A. Fourier-Transform Infrared study of the nematic order in thermotropic main-chain polyesters. *J. Polym. Sci. Pol. Phys.* **24**, 827–837 (1986).
36. Wang, X. et al. Revealing intermolecular interaction and surface restructuring of an aromatic thiol assembling on Au(111) by tip-enhanced Raman Spectroscopy. *Anal. Chem.* **88**, 915–921 (2015).
37. Kang, W.-S., Choi, S.-W., Kim, H.-S., Kim, J.-H. & Lee, J.-H. Raman spectroscopic comparison of zearalenone and its derivatives for non-destructive rapid detection. *J. Anal. Sci. Technol*. **15**, 34 (2024).
38. Sundholm, D. et al. Nuclear magnetic shieldings of stacked aromatic and antiaromatic molecules. *J. Chem. Theory Comput.* **13**, 1952–1962 (2017).
39. Ellis, J. E. Metal carbonyl anions: from $[Fe(CO)_4]^{2-}$ to $[Hf(CO)_6]^{2-}$ and beyond. *Organometallics* **22**, 3322–3338 (2003).
40. López-Tobar, E., Hara, K., Izquierdo-Lorenzo, I. & Sanchez-Cortes, S. Plasmonic effects of phenylenediisocyanides linked at interparticle junctions of metal nanoparticles. *J. Phys. Chem. C.* **119**, 599–609 (2014).
41. Tavakoli-Azar, T., Mahjoub, A. R., Sadjadi, M. S., Farhadyar, N. & Hossaini Sadr, M. The effect of temperature on the formation of $CdTiO_3$ structures for enhancing photocatalytic property. *Chem. Phys. Lett*. **755**, 137779 (2020).
42. Švančárek, P., Klement, R. & Galusek, D. Photoluminescence of $(ZnO)_{X-Z}(SiO_2)_Y$:$(MnO)_Z$ green phosphors prepared by direct thermal synthesis: The effect of ZnO/SiO_2 ratio and Mn^{2+} concentration on luminescence. *Ceram. Int.* **42**, 16852–16860 (2016).
43. Caspar, J. V., Kober, E. M., Sullivan, B. P. & Meyer, T. J. Application of the energy gap law to the decay of charge-transfer excited states. *J. Am. Chem. Soc.* **104**, 630–632 (1982).
44. Wilson, J. S. et al. The energy gap law for triplet states in Pt-containing conjugated polymers and monomers. *J. Am. Chem. Soc.* **123**, 9412–9417 (2001).
45. Gierschner, J., Ehni, M., Egelhaaf, H.-J., Medina, B. M. & Beljonne, D. Solid-state optical properties of linear polyconjugated molecules: π-stack contra herringbone. *J. Chem. Phys.* **123**, 144914 (2005).
46. Narouz, M. R. et al. Robust, highly luminescent Au13 superatoms protected by N-heterocyclic carbenes. *J. Am. Chem. Soc.* **141**, 14997–15002 (2019).
47. Bunz, U. H. et al. Synthesis and properties of functional twisted tolanes. *Chem. -Eur. J.* **23**, 9908–9918 (2017).
48. Gaschard, M., Nehzat, F., Cheminel, T. & Therrien, B. Arene Ruthenium Metalla-assemblies with anthracene moieties for PDT applications. *Inorganics* **6**, 97 (2018).
49. Ermolaev, N. L. et al. Tris(trifluoromethyl)germylethynyl derivatives of biphenyl and anthracene: Synthesis, structure, and evidence of the intramolecular charge transfer on the germanium center. *J. Organomet. Chem.* **797**, 83–95 (2015).
50. Patrick, C. W. et al. Masked alkynes for synthesis of threaded carbon chains. *Nat. Chem.* **16**, 193–200 (2024).

Acknowledgements

We thank the financial support from the National Natural Science Foundation of China (22371280 and 92261109), the National Key R&D program of China (2021YFA1502300), the Youth Innovation Promotion Association CAS (2021302), the CAS Youth Interdisciplinary Team, and the Self-Deployment Project Research Program of Haixi Institutes, Chinese Academy of Sciences (No. CXZX-2022-GH10).

Author contributions

W.W. and J.R.L. conceptualized the project, designed the experimental protocol, and drafted the initial manuscript. J.R.L. conducted the experiments and performed the data analysis. L.Z., Z.N.C., and S.J.N. performed DFT calculations and conducted the theoretical analysis. T.C. and Z.A.N. conducted the search and analysis in the CCDC database for the crystal structure of alkyne-π. Z.A.N. contributed to solving the issue of structural refinement. L.Y.L. contributed to NMR data analysis. Q.L. and Z.Z. helped with experimental design. WW. and Y.G.H. supervised the project. All authors revised the manuscript and approved the final version.

Competing interests

The author declares no competing interests.

Additional information

Supplementary information The online version contains supplementary material available at https://doi.org/10.1038/s42004-025-01792-9.

Correspondence and requests for materials should be addressed to Wei Wang, Lu Zhang or You-Gui Huang.

Peer review information *Communications Chemistry* thanks Stephen Argent and the other anonymous reviewers for their contribution to the peer review of this work. A peer review file is available.